

# Electronvolt energy resolution with broadband ptychography

Silvia Cipiccia<sup>\*a</sup>, Wiebe Stolp<sup>+b</sup>, Luca Fardin<sup>+a</sup>, Ralf Ziesche<sup>c</sup>, Ingo Manke<sup>c</sup>, Matthieu Boone<sup>b</sup>, Chris Armstrong<sup>d</sup>, Joachim R. Binder<sup>e</sup>, Nicole Bohn<sup>e</sup>, Alessandro Olivo<sup>a</sup>, and Darren Batey<sup>f</sup>

<sup>a</sup>Department of Medical Physics and Biomedical Engineering, University College London, Malet Place Engineering, Gower St, London, WC1E 6BT, United Kingdom

<sup>b</sup>UGCT-RP, Department of Physics and Astronomy, Ghent University, Ghent 9000, Belgium

<sup>c</sup>Helmholtz-Zentrum Berlin für Materialien und Energie Hahn Meitner Platz 1, 14109, Berlin, Germany

<sup>d</sup>Central Laser Facility, Rutherford Appleton Laboratory, Harwell Campus, Didcot OX11 0QX, United Kingdom

<sup>e</sup>Institute for Applied Materials, Karlsruhe Institute of Technology, Hermann-von-Helmholtz-Platz 1, 76344 Eggenstein-Leopoldshafen, Germany

<sup>f</sup>Diamond Light Source, Harwell Science and Innovation Campus, Fermi avenue, Didcot, OX110DE, United Kingdom

September 9, 2024

## Abstract

Ptychography is a scanning coherent diffraction imaging technique successfully applied in the electron, visible and x-ray regimes. One of the distinct features of ptychography with respect to other coherent diffraction techniques is its capability of dealing with partial spatial and temporal coherence via the reconstruction algorithm. Here we focus on the temporal and clarify the constraints which affect the energy resolution limits of the ptychographic algorithms. Based on this, we design and perform simulations for a broadband ptychography in the hard x-ray regime, which enables an energy resolution down to 1 eV. We benchmark the simulations

---

\*corresponding author: s.cipiccia@ucl.ac.uk

+These authors contributed equally to this work

against experimental ptychographic data of an NMC battery cathode material, attaining an energy resolution of 5 eV. We review the results, discuss the limitations, and provide guidelines for future broadband ptychography experiments, its prospective application for single acquisition x-ray absorption near edge structure imaging, magnetic dichroism imaging, and potential impact on achieving diffraction limited resolutions.

## 1 Introduction

Coherent diffraction imaging (CDI) techniques have opened the doors to diffraction limited resolutions by replacing the image forming lens with an algorithm [15, 28, 21, 17] to solve for the phase problem. Achieving such high resolution is reliant upon an high quality illumination, namely high coherence. Understanding how to extract the maximum information from the available coherent flux is critical to the development of ptychography and to push the limits of resolution across all imaging regimes. The coherence requirements for CDI are explained with clarity by Spence and collaborators [30] in their 2004 article in terms of lateral (spatial) and longitudinal (temporal) coherence.

Ptychography is a scanning CDI technique [26], where an object is scanned across the illumination at overlapping steps while recording diffraction patterns in the far field. By means of scanning, ptychography synthetically extends the lateral coherence length to match the object size. Nellist et al. in the electron regime [24], and later Thibault and Menzel in the x-ray regime [31], showed that the additional constraints in the object plane provided by the scanning process, can be used to relax the spatial coherence requirements. If the lateral coherence length is shorter than the illumination width, the partially coherent illumination can be interpreted as a mix of fully coherent states (or modes), incoherent to each other, and each independent mode can be recovered. This approach has enabled ptychography to deal with experimental issues such as a large source size or mechanical vibrations in the setup[18], making ptychography a robust experimental technique.

Further to the spatial coherence, ptychography has been proven to deal also with partial temporal coherence, such as the presence of multiple energies or broadband radiation [14, 32, 22]. This was first achieved by Batey et al. in their ptychographic imaging multiplexing (PIM) approach [7], by splitting the broadband illumination into discrete energy channels. Each energy channel acts as an independent measurement, and all the channels add together incoherently at the detector. Each energy has its own probe and object, this allows to take into account the difference in response that the sample may have to different energies. To give a practical example, let us consider the case where the sample is made out of nickel (Ni) and the illumination contains two discrete energies, one above and one below the Ni k-edge. The object corresponding to the energy channel above the edge will be more absorbing than the object corresponding to the energy channel below the edge. It is worth noting here that the approximation of a single object and multiple energies is possible in the assumption

the sample response is constant within the energy bandwidth (e.g. far from any absorption edge) [32].

To understand how the algorithm separates the energy states, we can picture the process as a cryptography problem: the various states are transferred through the same data channels (detector pixels) by encoding them through a key. That key is described by the illumination structure and scan position diversity. In order to encode the maximum information one must engineer a strong key, however solving for a strong key places a greater reliance on the initialisation. In Ref. [7] the decoding was achieved by initialising the energy channels from a measured monochromatic illumination. Undoubtedly this approach gives the possibility of relaxing the temporal coherence requirements Spence described for standard CDI, as proven in previous works [32, 22, 29]. However, there remains a lack of clarity as to what makes a good key for decoding the energies and what determines the energy resolution. For example, is it possible to achieve eV energy separations and enable single acquisition x-ray absorption near edge structure (XANES) imaging using a broadband spectrum? In this manuscript we aim to answer these questions via simulations and experimental results and provide guidance for future developments and applications of multi-energy ptychography.

## Reciprocal and real space constraints for energy resolving ptychographic imaging

The starting point of our study is the paper by Spence [30] and, without delving into the derivation which can be found in Ref [30], we report the key definitions and formulas upon which our work is built. A standard CDI setup is shown in Fig.1-a. The lateral (spatial) coherence length  $L_c$  at a given distance  $Z$  from the source is given by the Van-Cittert-Zernike theorem:  $L_c = \lambda Z/S$ , where  $\lambda$  is the wavelength and  $S$  is the source size. For imaging an object of width  $W$ , the spatial coherence requirement is given by  $L_c > 2W$  [30]. The longitudinal (temporal) coherence length  $L_t$  depends on the radiation energy  $E$  and its bandwidth  $\delta E$ :  $L_t = \lambda E/\delta E$ . Assuming the spatial coherence requirement is satisfied, Spence clarifies the longitudinal coherence will set the resolution,  $d_S$ , to be:

$$d_S = \frac{W\delta E}{E}. \quad (1)$$

Regarding the reconstructed pixel size  $\Delta x$ , in the conventional CDI sampling condition, this depends on the scattering angle subtended by the detector as well as the wavelength of the radiation and it is given by:

$$\Delta x = \frac{\lambda L}{D} = \frac{\lambda}{\theta} \quad (2)$$

where  $L$  is the sample-detector distance,  $D$  the width of the detector active area, and  $\theta$  the scattering angle covered by the detector (see Fig.1-a). The best resolution,  $d_{min}$ , depends on the maximum angle  $\theta_{max}$  at which the diffracted

photons are detected, it is affected by multiple factors, e.g. photon statistics, detector noise, scattering properties of the sample, and it is at best  $d_{min} = 2\Delta x$ . Based on the Eq. 1, as long as the energy bandwidth satisfies the condition:

$$\delta E < \frac{d_{min} E}{W} \quad (3)$$

the partial temporal coherence does not affect the achievable resolution. Otherwise, the best resolution is limited to  $d_S$ .

For the algorithm to succeed to separate multiple energies, their presence needs to be associated to a detectable difference, either in reciprocal space (detector plane) or in the real space (sample plane). To be detectable in the reciprocal space it means  $\theta_{max} > \lambda/d_S$ , which is equivalent to say  $d_S > d_{min}$ . To be detectable in the sample plane the illumination has to be different for each energy, and the difference has to be larger than  $d_{min}$ . To demonstrate these intuitive statements with practical examples, we perform a series of multi-energies simulations.

## Simulations

For simplicity, we start the study with a polychromatic beam made of two discrete energies and we perform two sets of simulations, the first with achromatic and the second with chromatic illumination. The simulations reported in this manuscript are performed using Diffractio [27], a python library for diffraction and interference optics. To make the energy separation clear, the two sample responses to the two energies are simulated by generating two different Siemens stars (100% transmission, 2 rad phase, e.g. see Fig. 2-A). The ptychography reconstructions are performed with an implementation of the ePIE algorithm [20] in PtyREX [5], including the ptychographic multiplexing approach [7]. To generate the dual-energy datasets, for each energy  $E_1$  and  $E_2$  we performed an independent simulation by scanning the object in a  $5 \times 5$  grid at steps of  $1 \mu\text{m}$ . Details regarding the illumination size at the samples are given in the following sections. The diffraction patterns for single energies are combined incoherently at each scanning step, by summing the intensities recorded at the detector plane.

### Achromatic setup

The simulated achromatic ptychography setup is shown in Fig.1-B). A circular illumination with diameter  $W = 5 \mu\text{m}$  is scanned across a sample. The diffraction pattern is recorded on a detector of width  $D$  at a distance  $L$ . The illumination at the sample is identical for the two energies  $E_1$  and  $E_2$  in terms of phase front and modulus, as produced by a pinhole.  $E_1 = 10 \text{ keV}$  is kept constant and  $E_2$  is varied between 10.01 and 13 keV. The list of simulated energies  $E_2$ , the corresponding energy differences  $\Delta E = E_2 - E_1$ , the calculated energy spread limited resolution  $d_S$  based on Eq. 1, and the details of the geometry are summarised in Table 1. The results are shown in Figure 2. For the reconstruction of the dual-energy datasets we used as initial estimates the probes retrieved from

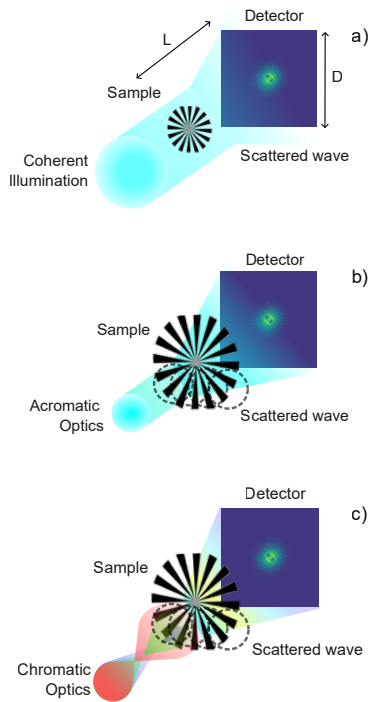


Figure 1: a) Standard CDI setup. A coherent illumination is diffracted by the sample. A detector at distance  $L$  records the diffraction patterns. b) Achromatic ptychography setup. An achromatic optics forms an energy independent illumination at the sample. c) Chromatic ptychography setup. A chromatic optics forms an energy dependent illumination at the sample. In b) and c) the sample is scanned through the illumination while a detector records the diffraction patterns.

Table 1: Simulated  $E_2$  energies and corresponding expected resolution limit based on Eq.1 and summary of the simulations parameters for the achromatic case.

$E_2$ [keV]	$\Delta E$ [keV]	$d_S$ [nm]
13.0	3	1150
11.0	1	455
10.1	0.1	49
10.01	0.01	5
Illumination at sample		5 $\mu\text{m}$
Scanning step		1 $\mu\text{m}$
Sample-detector distance		5 m
Detector pixel size		62 $\mu\text{m}$
Detector width		256 pixels
* $d_{min}$		76 nm

\*  $d_{min} = 2\Delta x$  Calculated for 10 keV, based on Eq.2

the single energy. The algorithm separates  $E_2 = 13$  and 11 keV from  $E_1 = 10$  keV (Figure 2 A-B). Some residual mix between the two energies is observed for  $E_2 = 10.1$  keV (Figure 2 C), while the separation fails for  $E_2 = 10.01$  keV (Figure 2 D). Having simulated an achromatic illumination, there is no difference for  $E_1$  and  $E_2$  in sample plane. The code can rely only on detectable difference in the detector plane. Therefore, the energy separation is achieved if

$$\frac{d_S}{d_{min}} > 1, \quad (4)$$

and fails otherwise (see Figure 2-E and -F). To go further in energy resolution a stronger key is needed. In the next section we explore the effects of introducing diversity in the probes at the different energies using chromatic optics.

### Chromatic setup

To study the chromatic case, we simulate Fresnel zone plates (FZPs) as the pre-sample focusing optics, as their chromatic behaviour is well understood and easily controllable. A Fresnel zone plate is a circular diffraction grating made of concentric alternating opaque and transparent rings, and it is one of the most common chromatic optics used in x-ray ptychography. The main parameters defining the properties of the optics are the radius  $R_{FZP}$ , and the outer zone width  $\Delta r$ , which determine the number of zones  $N$  and the focal length  $f$  [2]:

$$N = \frac{R_{FZP}}{2\Delta r} \quad (5)$$

$$f = \frac{4N(\Delta r)^2}{\lambda} \quad (6)$$

From the above, given a variation in wavelength  $\Delta\lambda$  the corresponding change

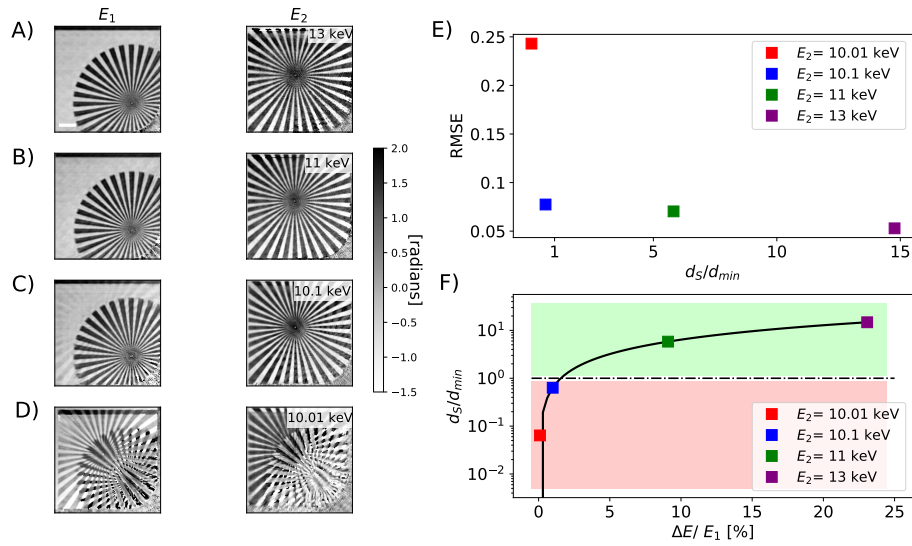


Figure 2: A-D) Retrieved phase object for  $E_1$  and  $E_2$  for different energy separation from 3 keV to 10 eV. The scale bar in A) corresponds to 1  $\mu\text{m}$  and applies all the figures A-D. E) RMSE for the retrieved phase object at  $E_1$  between the mixed energies and the monochromatic reconstruction. F) Calculated  $d_s/d_{min}$  for 10 keV as a function of the energy spread  $\Delta E/E_1$  from Eq. 1.

Table 2: Summary of the simulation parameters for the chromatic simulations: difference in probe size at the sample for different FZPs and energies and  $d_{min}$ .

$R_{FZP}$ [ $\mu\text{m}$ ]	$\Delta E = 10 \text{ eV}$		$\Delta E = 1 \text{ eV}$	
	$\Delta p$ [nm]	$d_{min}$ [nm]	$\Delta p$ [nm]	$d_{min}$ [nm]
20	1) 45	76	-.	-.
	2) 45	38	-.	-.
50	3) 105	38	5) 10	38
200	4) 400	76	6) 40	76
	-.	-.	7) 40	38
400	-.	-.	8) 80	76
	-.	-.	9) 80	38

in focal length  $\Delta f$  is:

$$\Delta f = -\frac{2R_{FZP}\Delta r}{\lambda^2}\Delta\lambda \quad (7)$$

Equation 7 shows that  $\Delta f$  increases linearly with the radius of the lens, hence a larger lens has a stronger chromaticity for the same  $\Delta r$ . We performed a set of chromatic simulations for  $E_2 = 10.01$  and  $10.001$  keV, while keeping  $E_1 = 10$  keV, to explore the energy separation not resolved by the achromatic setup. For all the simulations the  $E_1$  beam size at the sample is  $5 \mu\text{m}$  and the scanning step size is  $1 \mu\text{m}$ . The calculated difference in beam size  $\Delta p$  for the  $E_2$  energies with respect to  $E_1$  for four different  $R_{FZP}$  are summarised in Table 2. We have varied  $d_{min}$  by cropping the detector active area, that is varying the number of pixels used for the reconstruction (between  $512 \times 512$ , full detector, and  $256 \times 256$  pixels).

For each entry of Table 2 (numbered 1-9) we performed a simulation using the sample-detector distance and detector specifications listed in Table 1. In the reconstructions, unlike for the achromatic setup, the probe retrieved from the monochromatic case was not used as an initial estimate, as modelling the FZP as pre-focusing optics was sufficient. The results of the simulations are shown in Figure 3A. Using the  $20 \mu\text{m}$  radius FZP,  $10 \text{ eV}$  separation fails for  $256$  cropping ( $d_{min} = 76 \text{ nm}$ ), while it is achieved with  $512$  cropping ( $d_{min} = 38 \text{ nm}$ ). The  $10 \text{ eV}$  separation is fully achieved with both the  $50$  and the  $200 \mu\text{m}$  radius FZP with  $d_{min} = 76 \text{ nm}$  and  $d_{min} = 38 \text{ nm}$  respectively. The  $400 \mu\text{m}$  radius FZP successfully separates  $1 \text{ eV}$ . Figure 3B presents the results in terms of root mean square error (RMSE) between the PIM reconstructions and the single energy reconstructions by plotting the RMSE as a function of the ratio  $\Delta p / d_{min}$ . Figure 3C summarises the same results in terms of success and failure by plotting the value of the ratio  $\Delta p / d_{min}$  for the different configurations:  $> 1$  "success",  $< 1$  "failure". Summarising, by using a pre-sample chromatic optics in the ptychography setup, the probe at the sample is different for different energies. If this difference is detectable, that is:

$$\frac{\Delta p}{d_{min}} > 1, \quad (8)$$



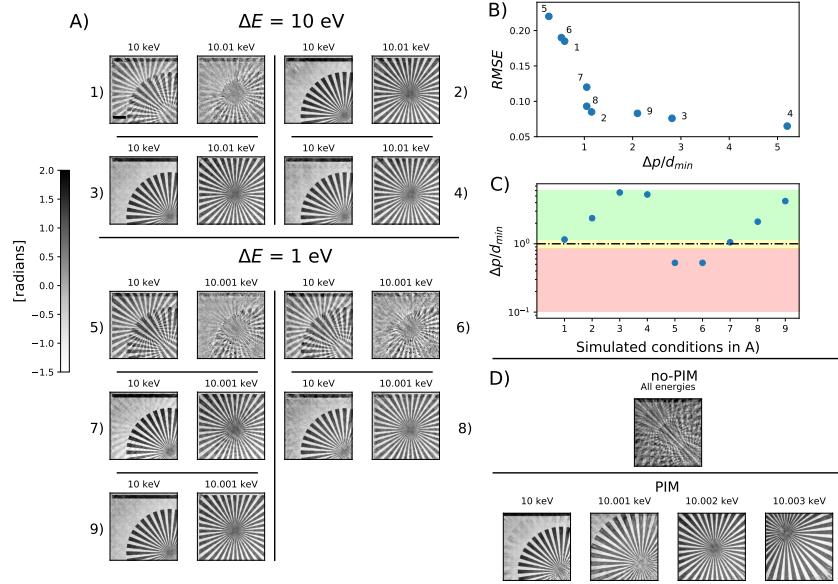


Figure 3: A) 1-9 PIM Retrieved object phase for  $E_1$  and  $E_2$  for different  $R_{FZP}$  and different  $\Delta E$ . B) RMSE for the retrieved object phase at  $E_1$  between the single energy and the mixed energies retrieval, as a function of the ratio  $\Delta p/d_{min}$ . C) Visualization of the success/failure in energy separation of the algorithm for the different conditions A)1-9 in respect to the  $\Delta p/d_{min}$  ratio. D) Simulations for four energies. Retrieved phase image using PIM and without PIM. The scale bar in A-1) corresponds to  $1 \mu\text{m}$  and applies to all the figures in A and D.

the algorithm can separate/decode the energies, even if the condition of Eq.4 is not satisfied.

Up to here we have simulated a polychromatic beam made of two energies only. The capability of the PIM approach to separate more than two energies has already been proven in previous works [32, 7]. To confirm this is still the case for a very fine energy separation (1eV at 10 keV, hence at 0.01% B.W.), we performed a set of simulations where the diffraction patterns of four different objects corresponding to four energies between 10 and 10.003 keV at steps of 1eV are combined together. The sample is in this case scanned in a  $10 \times 10$  grid at steps of  $0.5 \mu\text{m}$  to provide the algorithm enough conditions to solve for all the four complex objects and illuminations. The results are shown in Figure 3-D, where different phase objects are retrieved for each energy and compared with the reconstruction obtained for the single energy approximation (single energy mode). The separation is reached, despite some residual energy mix still visible in the retrieved objects.

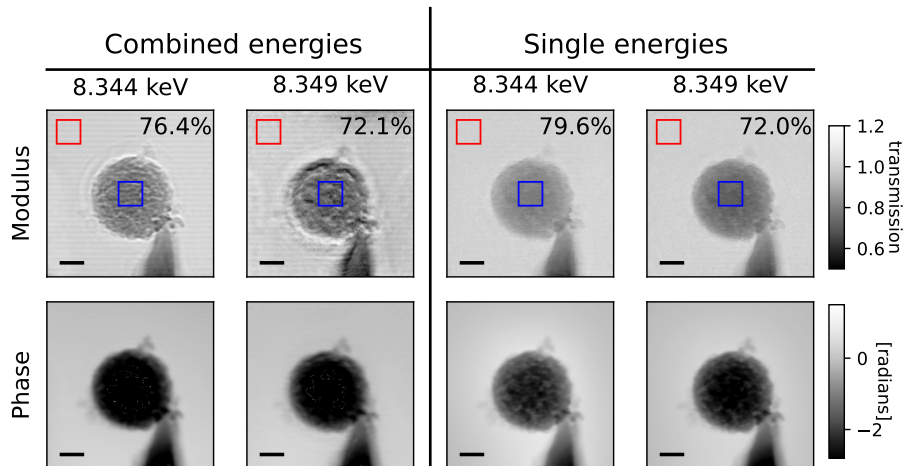


Figure 4: Retrieved modulus and phase images of an NMC sample from an experimental acquisition with single and combined energies. For all the reconstructions two spatial modes were used to compensate for the blurring introduced by the continuous sample motion. The transmission is calculated as a ratio between the average pixel value in the sample (blue box) and the average pixel value in air (red box). The scale bar corresponds to 2  $\mu\text{m}$

## Experiment

The condition expressed by Eq.8 finds experimental confirmation in published results available in literature by Yao et al. [32] where a FZP with 90  $\mu\text{m}$  radius, 50 nm outer-most zone width, was used as focusing optics to illuminate a sample with broadband radiation centred at 8.8 keV. Using the energy separation of the ptychographic algorithm they improved the image resolution down to a measured spatial resolution of  $d_{min} = 30$  nm and 25 eV energy separation. In their study the variation in illumination size at the sample for 8.8 keV and 8.825 keV was  $\Delta p \approx 500$  nm  $\gg d_{min} = 30$  nm (see Figure 4 in Ref. [32]). Therefore, the experimental conditions were satisfying the requirement given by Eq.8 for a successful energy separation. The sample was a gold Siemens star test pattern, which has a quasi-achromatic behaviour across the bandwidth of the experiment, since the x-ray energies are far enough from any gold absorption edge. Because of this in Ref [32] the sample behaviour was approximated to a single object (achromatic) for all the different energy channels.

To quantify the sensitivity of the algorithm in energy separation a chromatic sample is needed. Therefore, we have performed an experiment to image NMC-622 ( $\text{LiNi}_{0.6}\text{Mn}_{0.2}\text{Co}_{0.2}\text{O}_2$ ) active battery cathode material across the Ni absorption k-edge. The experiment was performed at the I13-1 beamline of Diamond Light Source[3]. ). For the experiment a NMC secondary particle was mounted on the top of a syringe needle using a FIB-SEM to position and mount

the cathode material particle. A set of blazed FZP [16], 400 $\mu\text{m}$  radius and 100 nm outer most ring, were used to create an illumination at the sample of 4.0  $\mu\text{m}$  at 8.344 keV. The x-ray beam energy was scanned across the Ni k-edge by using a double crystal Si-111 monochromator available at the beamline (bandwidth  $10^{-4}$ ). The sample was scanned in a regular grid at steps of 0.25  $\mu\text{m}$  and 0.5 $\mu\text{m}$  in the horizontal and vertical direction respectively, in fly-scanning mode [4] (see supplementary material). The diffraction patterns were recorded 5.7 m downstream the sample using an EIGER 500k photon counting detector (75  $\mu\text{m}$  pixel size,  $1028 \times 512$  pixels, 2 ms exposure time). We acquired two separate datasets, at 8.344 and 8.349 keV, that is above and below the 8.346 keV Ni<sub>2</sub> absorption k-edge (to be noticed this is higher than for pure Ni k-edge, see supplementary material). In the experimental configuration, the FZP produced a beam size at the sample of approximately 3.5  $\mu\text{m}$  at 8.349 keV, corresponding to a  $\Delta p \approx 500$  nm. We first reconstruct the two acquisitions separately for the two energies using 1000 iterations of PtyREX code[5] and two spatial modes to compensate for the blurring (partial coherence) due to the fly-scanning[4]. We estimated the resolution of the single energy image via Fourier ring correlation (see supplementary material) to be  $d_{min} = 200$  nm, which is smaller than  $\Delta p$  and satisfies the condition in Eq.8. We generated a mixed-energy dataset by summing the diffraction patterns separately recorded for the two energies at each scanning position. We used the retrieved probes from the single-energy reconstructions as initial estimates for the combined energy (PIM) reconstruction (1000 iterations, two spatial modes, and two energy channels). The retrieved object modulus and phase for single and mixed energies are shown in Figure 4. In the PIM reconstruction, despite some residual mixing being present in the two retrieved objects, with more pronounced grid artefacts compared to the single energy ones, the Ni edge is successfully identified, within a 3% error.

## Discussion and Conclusions

We have investigated the limits in energy resolution of the ptychographic imaging multiplexing approach. We clarified via simulations and experimental results that, in order for the algorithm to succeed in separating multiple energies, the effect of the polychromaticity has to be detectable either in the detector (reciprocal space) or in the sample (real space) plane. High energy resolution, e.g.  $< 1\text{eV}$ , can be achieved by engineering high chromaticity optics combined to a broadband illumination, and a good knowledge of the chromatic illumination. This prior-knowledge is used to seed the starting point of the PIM reconstruction and it can be obtained either via accurate modelling of the optics within the algorithm or by using the illumination retrieved from monochromatic acquisitions. In our study we have used a FZP, which is a common optic used in x-ray ptychography and easy to model within the algorithm. However, the findings can be extended to any other chromatic optics and are not limited to FZPs. In the reported experiment, the broadband was emulated by adding together, at each scanning position, monochromatic diffraction patterns. This

process is based on the assumption the scanning positions are identical for the two monochromatic acquisitions. As the acquisitions were in fly-scanning mode, the positions are expected to be similar but not identical and we believe this hindered the full energy separation in the PIM reconstruction, together with the presence of Poisson noise, which was not added in the simulations. It is important also to notice that the experimental data is based on discrete energies. While Yao[32] has shown it is possible to apply the multiplexing approach to a continuous spectrum, the energy resolution and whether the quantitiveness of PIM method hold when going from the discrete to the continuum, still needs to be verified.

The study is based on the PIM approach implemented in PtyREX code, yet we do not expect the results to be code dependent. We have investigated the broadband ptychography robustness focusing on the x-ray regime, however, we expect the findings to be valid at any wavelength and radiation. The focus on the x-ray regime is driven by prospective applications for x-ray dichroic and XANES imaging. Ptychography has been proven to be instrumental for magnetic dichroic imaging [13, 12, 19] and XANES imaging [25, 33]. Both techniques require energy scans with steps as small as 1 eV. Based on the findings and the simulations results, 1 eV energy separation is within reach with broadband ptychography, by designing an experimental setup that satisfies the Eq.8. This would be transformative in terms of reducing the acquisition time and producing inherently co-registered nano scale images across energies. Concerning how to produce a broadband illumination, a multilayer crystal monochromator allows to select bandwidths up to a few percent [9]. For experimental settings based on undulator sources, the width of the undulator harmonics can be matched to the bandwidth of the multilayer monochromator by tapering the undulator [23, 6].

In laboratory settings [8], because of the lower flux, the role of the monochromator can be replaced with an energy thresholding [10] or resolving detector [6]. By combining such detectors with an appropriate chromatic optics and the PIM approach, it would be possible to go beyond the energy resolution of the detector itself.

As a final note regarding the potential impact of this study on reaching diffraction limited resolution, recently a 4 nm resolution record has been demonstrated [1] for hard x-ray ptychography (6.2 keV, 0.02% B.W.). However, the diffraction limit remains over an order of magnitude lower. Based on the scaling of flux vs resolution presented by Deng et al. [11], one order of magnitude increase in flux on the sample corresponds to an increase of a factor two in resolution. Therefore, about  $10^5$  times more flux than in Ref. [1] would be required to approach the diffraction limit. The experiment in Ref. [1] was performed at a third generation light source, yet even with the upgrade to a fourth generation light source, this flux enhancement remains out of reach. One solution would be to exploit a broader energy bandwidth (few %s), e.g. with a multilayer monochromator. However, the broad bandwidth itself would hinder the resolution. The combination of higher flux, chromatic optics to satisfy Eq. 8, and the PIM reconstruction approach could be the key to unlock diffraction limited x-ray ptychography.

## Acknowledgements

The Authors thank the Diamond Light Source for the proposal MG30867-1 and MG36318-1. This work is supported by EPSRC New Investigator Award EP/X020657/1 and Royal Society RGS/R1/231027. A.O. is supported by the Royal Academy of Engineering: CiET1819/2/78. Parts of the study were supported by the German BMWK project HiBrain (03ETE039G).

## References

- [1] T. Aidukas, N. W. Phillips, A. Diaz, E. Poghosyan, E. Müller, A. F. J. Levi, G. Aeppli, M. Guizar-Sicairos, and M. Holler. High-performance 4-nm-resolution x-ray tomography using burst ptychography. *Nature*, 632(8023):81–88, 2024.
- [2] D. Attwood. *Soft X-ray microscopy with diffractive optics*, page 337–394. Cambridge University Press, 1999.
- [3] D. Batey, S. Cipiccia, X. Shi, S. Williams, K. Wanelik, A. Wilson, S. Pérez-Tamarit, P. Cimavilla, M. A. Rodríguez-Pérez, and C. Rau. Coherence Branch at I13, DLS: The Multiscale, Multimodal, Ptycho-tomographic End Station. *Microscopy and Microanalysis*, 24(S2):40–41, 08 2018.
- [4] D. Batey, C. Rau, and S. Cipiccia. High-speed x-ray ptychographic tomography. *Scientific Reports*, 12:7846, 2022.
- [5] D. J. Batey. Ptychographic imaging of mixed states, 2014. PhD thesis.
- [6] D. J. Batey, S. Cipiccia, F. Van Assche, S. Vanheule, J. Vanmechelen, M. N. Boone, and C. Rau. Spectroscopic imaging with single acquisition ptychography and a hyperspectral detector. *Scientific Reports*, 9:12278, 2019.
- [7] D. J. Batey, D. Claus, and J. M. Rodenburg. Information multiplexing in ptychography. *Ultramicroscopy*, 138:13–21, 2014.
- [8] D. J. Batey, F. Van Assche, S. Vanheule, M. N. Boone, A. J. Parnell, O. O. Mykhaylyk, C. Rau, and S. Cipiccia. X-ray ptychography with a laboratory source. *Phys. Rev. Lett.*, 126:193902, May 2021.
- [9] M. N. Boone, F. Van Assche, S. Vanheule, S. Cipiccia, H. Wang, L. Vincze, and L. Van Hoorebeke. Coherence and sampling requirements for diffractive imaging. *Journal Synchrotron Radiation*, 27:110–118, 2020.
- [10] F. Brun, V. Di Trapani, D. Batey, S. Cipiccia, and C. Rau. Edge-subtraction x-ray ptychographic imaging with pink beam synchrotron radiation and a single photon-counting detector. *Scientific Reports*, 10:6526, 2020.

- [11] J. Deng, Y. Yao, Y. Jiang, S. Chen, T. M. Mooney, J. A. Klug, F. S. Marin, C. Roehrig, K. Yue, C. Preissner, Z. Cai, B. Lai, and S. Vogt. High-resolution ptychographic imaging enabled by high-speed multi-pass scanning. *Opt. Express*, 30(15):26027–26042, Jul 2022.
- [12] C. Donnelly, K. L. Metlov, V. Scagnoli, M. Guizar-Sicairos, M. Holler, N. S. Bingham, J. Raabe, L. J. Heyderman, N. R. Cooper, and S. Gliga. High-resolution hard x-ray magnetic imaging with dichroic ptychography. *Nature Physics*, 17:316–321, 2021.
- [13] C. Donnelly, V. Scagnoli, M. Guizar-Sicairos, M. Holler, F. Wilhelm, F. Guillou, A. Rogalev, C. Detlefs, A. Menzel, J. Raabe, and L. J. Heyderman. High-resolution hard x-ray magnetic imaging with dichroic ptychography. *Phys. Rev. B*, 94:064421, Aug 2016.
- [14] B. Enders, M. Dierolf, P. Cloetens, M. Stockmar, F. Pfeiffer, and P. Thibault. Ptychography with broad-bandwidth radiation. *Applied Physics Letters*, 104(17):171104, 04 2014.
- [15] D. Gabor. A new microscopic principle. *Nature*, 161:777–778, 1948.
- [16] S. Gorelick, J. Vila-Comamala, V. A. Guzenko, R. Barrett, M. Salomé, and C. David. High-efficiency fresnel zone plates for hard x-rays by 100 keV e-beam lithography and electroplating. *Journal of Synchrotron Radiation*, 18:442–6, 2011.
- [17] W. Hoppe. Beugung im inhomogenen Primärstrahlwellenfeld. I. Prinzip einer Phasenmessung von Elektronenbeugungsinterferenzen. *Acta Crystallographica Section A*, 25(4):495–501, Jul 1969.
- [18] P. Li, T. Edo, D. Batey, J. Rodenburg, and A. Maiden. Breaking ambiguities in mixed state ptychography. *Opt. Express*, 24(8):9038–9052, Apr 2016.
- [19] Y. H. Lo, J. Zhou, A. Rana, D. Morrill, C. Gentry, B. Enders, Y.-S. Yu, C.-Y. Sun, D. A. Shapiro, R. W. Falcone, H. C. Kapteyn, M. M. Murnane, P. U. P. A. Gilbert, and J. Miao. X-ray linear dichroic ptychography. *Proceedings of the National Academy of Sciences*, 118(3):e2019068118, 2021.
- [20] A. M. Maiden and J. M. Rodenburg. An improved ptychographical phase retrieval algorithm for diffractive imaging. *Ultramicroscopy*, 109(10):1256–62, 2009.
- [21] J. Miao, T. Ishikawa, I. K. Robinson, and M. M. Murnane. Beyond crystallography: Diffractive imaging using coherent x-ray light sources. *Science*, 348(6234):530–535, 2015.
- [22] D. S. P. Molina, L. Loetgering, W. Eschen, J. Limpert, and J. Rothhardt. Broadband ptychography using curved wavefront illumination. *Opt. Express*, 31(16):26958–26968, Jul 2023.

- [23] D. A. Mossessian and P. A. Heimann. Characterization of ALS undulator radiation—High K, taper, and the near field effect. *Review of Scientific Instruments*, 66(11):5153–5161, 11 1995.
- [24] P. Nellist, B. McCallum, and J. Rodenburg. Resolution beyond the ‘information limit’ in transmission electron microscopy. *Nature*, 374(3):630–632, 1995.
- [25] A. Pattammattel, R. Tappero, M. Ge, Y. S. Chu, X. Huang, Y. Gao, and H. Yan. High-sensitivity nanoscale chemical imaging with hard x-ray nanoxanes. *Science Advances*, 6(37):eabb3615, 2020.
- [26] J. M. Rodenburg, A. C. Hurst, A. G. Cullis, B. R. Dobson, F. Pfeiffer, O. Bunk, C. David, K. Jefimovs, and I. Johnson. Hard-x-ray lensless imaging of extended objects. *Phys. Rev. Lett.*, 98:034801, Jan 2007.
- [27] L. Sanchez Brea. Diffractio, python module for diffraction and interference optics, 2019. <https://pypi.org/project/diffractio/>.
- [28] D. Sayre. Prospects for long-wavelength x-ray microscopy and diffraction. In M. Schlenker, M. Fink, J. P. Goedgebuer, C. Malgrange, J. C. Vieénot, and R. H. Wade, editors, *Imaging Processes and Coherence in Physics*, pages 229–235, Berlin, Heidelberg, 1980. Springer Berlin Heidelberg.
- [29] D. Schmidt, D. Goldberger, A. De Las Heras, C. Hernández-García, Y. Lei, P. Kazansky, D. Adams, and C. Durfee. Multiplexed broadband ptychography characterization of complex spatial and spectral euv beams from high harmonic generation. In *2022 Conference on Lasers and Electro-Optics (CLEO)*, pages 1–2, 2022.
- [30] J. C. Spence, U. Weierstall, and M. Howells. Coherence and sampling requirements for diffractive imaging. *Ultramicroscopy*, 101:929–936, 2004.
- [31] P. Thibault and A. Menzel. Reconstructing state mixtures from diffraction measurements. *Nature*, 494:68–71, 2013.
- [32] Y. Yao, Y. Jiang, J. Klug, Y. Nashed, C. Roehrig, C. Preissner, F. Marin, M. Wojcik, O. Cossairt, Z. Cai, S. Vogt, B. Lai, and J. Deng. Broadband x-ray ptychography using multi-wavelength algorithm. *Journal of Synchrotron Radiation*, 101:309–317, 2021.
- [33] X. Zhu, A. P. Hitchcock, D. A. Bazylinski, P. Denes, J. Joseph, U. Lins, S. Marchesini, H.-W. Shiu, T. Tyliczszak, and D. A. Shapiro. Measuring spectroscopy and magnetism of extracted and intracellular magnetosomes using soft x-ray ptychography. *Proceedings of the National Academy of Sciences*, 113(51):E8219–E8227, 2016.

# Supplementary Material

## Sample preparation

The NMC-622 sample was prepared at the Karlsruhe Institute of Technology (KIT) in Germany. For the experiment an NMC particle was mounted on the top of a syringe needle using a FIB-SEM to position and mount the particle. The needle was placed on the top of the scanning motor, a 3 axis MarsPI300 piezo stage. The sample was scanned in fly scanning mode as described in Ref. [1].

## k-edge for different Ni oxidation states

We measured the dependency of the k-edge as a function of the Ni oxidation state. The measurements are shown in Figure 1.

## Experimental image resolution estimation via FRC

Two consecutive acquisitions produced the two independent datasets used for calculating the Fourier ring correlation. The correlation between the two half datasets was compared to a half-bit information threshold, using an implementation based on van Heel et al. [4]. The resolution is 200 nm, see Figure 2.

## Fly-scanning ptychography

In a standard ptychographic acquisition, the sample is scanned across the illumination in step-and-shot mode: the sample is moved and, after a settling time required for the scanning motors to stabilise, an image is recorded by the detector. On the contrary, in fly scanning ptychography, the sample is moved continuously across the illumination while the detector acquires the diffraction patterns. This method allows to minimise the overheads [2] and enabling ultra-fast scanning[1]. The blurring effect due to the continuous motion can be compensated by using modal decomposition [3].



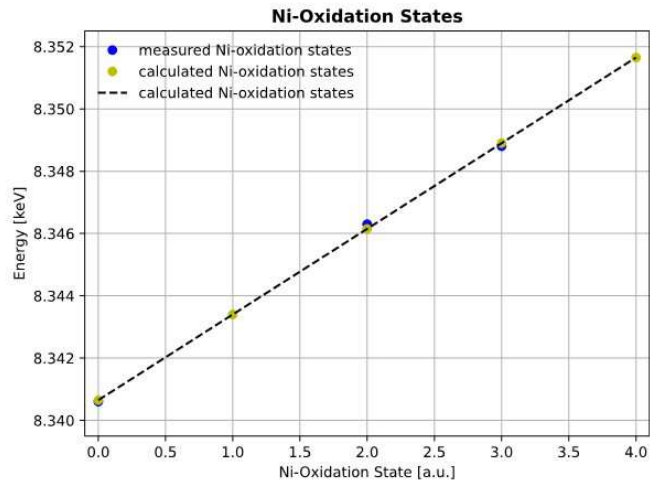


Figure 1: Measured k-edge variation as a function of the oxidation state.

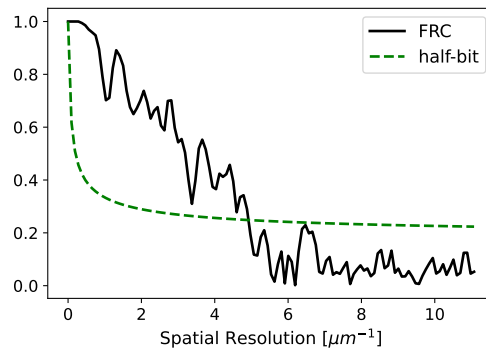


Figure 2: FRC for the 8.344 keV ptychographic reconstruction.

## References

- [1] D. Batey, C. Rau, and S. Cipiccia. High-speed x-ray ptychographic tomography. *Scientific Reports*, 12:7846, 2022.
- [2] P. M. Pelz, M. Guizar-Sicairos, P. Thibault, I. Johnson, M. Holler, and A. Menzel. On-the-fly scans for X-ray ptychography. *Applied Physics Letters*, 105(25):251101, 12 2014.
- [3] P. Thibault and A. Menzel. Reconstructing state mixtures from diffraction measurements. *Nature*, 494:68–71, 2013.
- [4] M. van Heel and M. Schatz. Fourier shell correlation threshold criteria. *Journal of Structural Biology*, 151(3):250–262, 2005.